New critical-state model for critical currents in ceramic high-T_c superconductors

H. Dersch and G. Blatter
Asea Brown Boveri, Corporate Research, CH-5405 Baden, Switzerland
(Received 17 June 1988)

Critical-current and magnetization measurements are performed on a large number of ceramic superconductors of the $YBa_2Cu_3O_7$ family. The results show that critical currents in present ceramics depend strongly on sample geometry and are, in fact, completely determined by self-field limitation. The strong magnetic field dependence leads to a general relation between critical current and magnetization which is experimentally found to be satisfied. A quantitative critical-state model based on an extension of Bean's theory is outlined which is able to predict transport and magnetic properties using microscopic current vs magnetic field relations. The underlying microscopic parameters are extracted from a comparison of the model calculation with measured transport and magnetization data.

I. INTRODUCTION

A vast amount of experimental data on the new oxide superconductors and many of their potential applications deal with polycrystalline material whose macroscopic properties are only indirectly related to microscopic properties like the actual mechanism producing superconductivity. The current transport and the magnetization of a bulk sintered sample are governed by the interplay of superconducting crystalline particles and their interconnections which establish the coherence within the sample. Many of the relevant effects of granularity have been studied for a long time on conventional superconductors[1] as well as, more recently,[2] on high-T_c superconductors (HTSC) and are by now fairly well established and understood.[3-5] However, the results of the theories are often local quantities which are valid on the (microscopic) scale of the grains, as for example the magnetic-field dependence of the critical current between two adjacent grains[6] or the pinning force of intergrain vortices.[5] In order to predict or analyze quantities of macroscopic samples or devices, it is necessary to calculate critical currents, magnetization, ac losses, etc., from local critical parameters. For conventional superconductors, this is usually done via Bean's[7] critical-state model which is used both as a design tool[8] and, on the other hand, to determine microscopic quantities from macroscopic measurements. In the case of the oxide superconductors, many researchers explicitly or implicitly use again Bean's model to analyze their data.[9,10] It turns out, however, that the relation between local and global quantities is more complex in the oxide superconductors. In this paper, we will present critical current measurements and ac magnetization data obtained at 77 K which show that Bean's original model is inadequate for the new polycrystalline superconductors, and, in fact, has to be substantially modified and extended. The reason for its failure is the strong magnetic-field dependence of the critical current which leads to current limitation in a macroscopic wire caused by the magnetic self-field. Our results show that transport in ceramic material with dimensions larger than 0.05 cm is always limited by this effect and never displays the underlying local critical current density j_c. Similarly, the magnetization displays a complex behavior and the extraction of the underlying microscopic parameters (e.g., the critical-current density) from magnetization experiments (inductively measured[11] j_c) has to be done more carefully than usual.

The paper is organized as follows: In Sec. II, we present the experimental results on the critical-current density and on the magnetic properties of our samples. In Sec. III, we will derive the phenomenological theory of granular superconductors and show how Bean's original model can be extended to the case of ceramic samples characterized by a strong field dependence of the critical current. Both magnetization and critical-current data are calculated within this extended model and good agreement with experimental results is obtained. In Sec. IV, we summarize our results and discuss the local relation between the critical current density j_c and the magnetic induction B as deduced from the experimental data. The calculation of the magnetic hysteresis is described in the Appendix.

II. EXPERIMENTS

The samples used in the present study are a large number of sintered ceramic pellets with the composition $R_1Ba_2Cu_3O_{7-\delta}$, where R=Y, Gd, Ho, and δ=0–0.2. The preparation conditions are different in each case and reflect an ongoing effort to optimize the material. Samples are single phased to 95% as judged from x-ray diffraction measurements. A variety of starting materials is used: (i) mixed, ground, reacted, and reground powders of the metal oxides, oxalates, or carbonates; (ii) coprecipitated powders of oxalates and tartrates. The highest critical-current density j_{crit}=900 A cm^{-2} at 77 K is obtained on a sample made from the tartrates by sintering at a temperature of 925 °C in oxygen atmosphere [we denote the macroscopic critical current density by j_{crit} whereas we use $j_c(B)$ for the microscopic (local) current-field relation]. The density of this sample is 97% of the theoretical density and the average grain size is well below 10 μm. Oxygen annealing at 450 °C is required to obtain the op-

timum stoichiometry.

The present study deals with common trends in the transport and magnetic characteristics of these samples. The most extensively studied material parameter, the critical temperature T_c, turns out to be rather insensitive to variations in sample preparation. We obtain $T_c = 92 \pm 5$ K with a resistive transition width (90%–10%) smaller than 2 K for all samples. The measurements described in the following are performed at 77 K with the sample immersed in liquid nitrogen.

A. Critical current

Current-voltage characteristics are measured in a four-point arrangement on pellet-shaped samples with a diameter of 1.2 cm and a thickness of 0.1 cm. The current is forced through a 0.1-cm constriction which is sawed into the round sample (see Fig. 1). Electric contacts are formed by scraping the sample and applying conductive silver paint. No burn-in is required as is with several methods described in the literature[12–14] which would make the test sample differ from the rest of the batch. The contact resistance is typically less than 10 $m\Omega\,cm^2$. The voltage drop which develops at the inner contacts is monitored as the current through the outer contacts is increased from 0 to 20 A. External magnetic fields can be varied between 0 T (i.e., earth magnetic field) and 1.5 T.

A typical result obtained on a medium-j_{crit} sample is shown in Fig. 2. The zero-field curve shows a notable voltage developing above 4 A. The nonlinear upturn in voltage finally goes over into a constant slope with a differential resistance about 10% of the normal resistance above T_c. Most samples exhibit this linear regime but there are some exceptions, most notably among the high-j_{crit} materials. The critical current is defined arbitrarily as the current where the voltage drop is 1 μV. It turns out that the j-V characteristic is rather steep and the critical current depends only weakly on this particular choice. For instance, requiring 0.1 μV voltage drop changes the critical current by at most 5%. The critical current decreases substantially upon application of rather weak magnetic fields: As can be seen from Fig. 2, j_{crit} is reduced by a factor of 10 at a field of only 100 Oe. Changing the field direction has only a minor influence on the current-voltage characteristic. This finding is typical for granular superconductivity.[15] In this as well as in the following measurements we always choose the perpendicular arrangement of current and magnetic field direction. Figure 3 exhibits the field dependence of the critical-current density for medium- and high-j_{crit} samples. A steep decrease at low fields followed by a leveling off at higher fields (> 100 Oe) is found. This behavior has been described in the literature.[11,16] The steep decrease is be-

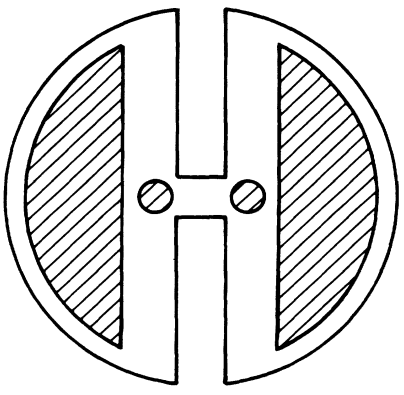

FIG. 1. Four-point arrangement and constriction on a sample for the determination of the critical-current density j_{crit}.

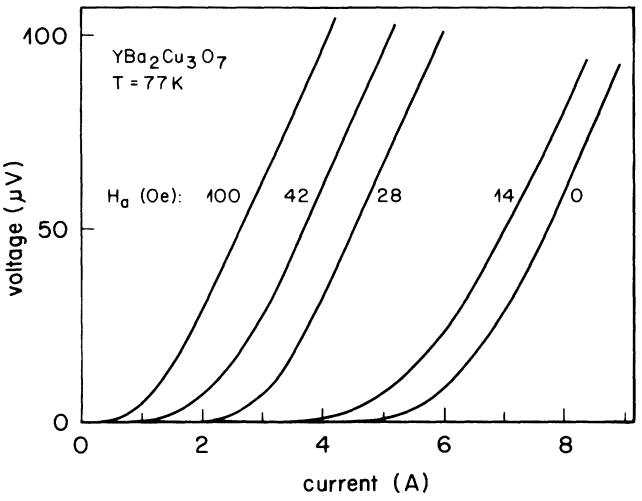

FIG. 2. Voltage drop across the constriction as a function of current density for different values of the applied magnetic field. The critical current is defined at the voltage drop of 1 μV. A weak magnetic field of the order of 100 Oe suppresses the critical current by one order of magnitude.

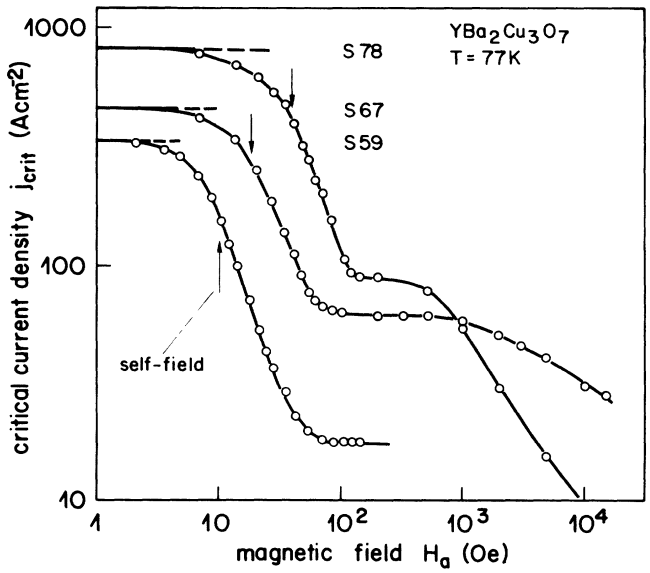

FIG. 3. Critical-current density as a function of applied magnetic field. The steep decrease of the current density with applied field is due to the weakly coupled grains. The saturation current may be due to a few percolating paths of strongly linked grains in the sample.

lieved to be due to weakly coupled grains and reflects the strong magnetic-field dependence of the dc Josephson effect.[16] Two important additional observations can be made: (i) The higher the critical current, the higher is the field of the initial drop in j_{crit}. (ii) The self-field at zero external field (see arrows in Fig. 3), i.e., the magnetic field due to the current at the edge of the constriction, is of the same order of magnitude as the field at which the critical current starts to decrease substantially. These findings give the first strong evidence for the hypothesis that *the self-field is in fact limiting the current carrying capability of the present samples via a local j_c vs B relation.*[17] To understand this effect we consider a simplified model: Suppose the material satisfies a local relation between the critical-current density j_c and the magnetic induction B such that

$$j_c = \begin{cases} j_0, & B < B^*, \\ 0, & B > B^*. \end{cases} \tag{1}$$

For a cylinder with radius R we obtain a total critical current which after normalizing to the cross section of the cylinder yields an apparent critical current density

$$j_{crit} = \begin{cases} j_0, & R < \dfrac{cB^*}{2\pi j_0}, \\ \dfrac{cB^*}{2\pi R}, & R > \dfrac{cB^*}{2\pi j_0}. \end{cases} \tag{2}$$

For large radii, specifically $R > cB^*/2\pi j_0$, j_{crit} does not depend on the local critical current j_0 but solely on the cutoff field B^*. As we will see below, the present samples are in this regime down to radii of 0.05 cm.

An important consequence and proof of this hypothesis is the dependence of j_{crit} on sample size: Equation (2) indicates an inverse relationship between current density and radius. Such behavior is indeed found in all of our samples; Fig. 4 gives a survey of the critical current observed in several samples as a function of the size of the constriction (see Fig. 1). We would like to emphasize that each curve represents one sample, the constriction being reduced after each measurement. Experimentally, we observe an increase in critical-current density with decreasing radius, in agreement with the predicted functional dependence [Eq. (2)]. No saturation at small radii can be seen. We conclude that the macroscopic critical current density is not a useful material parameter since it is not a geometry-independent property. In comparing results from different laboratories, effects due to sample size and shape have to be taken into account appropriately. In fact, some astonishingly high j_{crit} values found in the literature have been obtained on geometries giving favorable conditions. Favorable means that the macroscopic critical-current approaches the local critical-current density j_0 [Eq. (1)]. From basic electrodynamics it follows that an advantageous geometry is characterized by a large ratio of circumference to cross section. The worst situation is obviously a circular shape as is (roughly) used in the present study. Much larger critical-current densities are expected for thin filaments or thin films. Indeed, the highest reported j_{crit} values are found in such samples. We do not suggest that high j_{crit} values in epitaxial films are due to this self-field effect. This would be impossible since the magnetic field dependence of j_{crit} reported for epitaxial thin films is much weaker than in bulk ceramics. However, it may well be possible that some thin high-j_{crit} polycrystalline films perform well on the basis of the suggested mechanism.

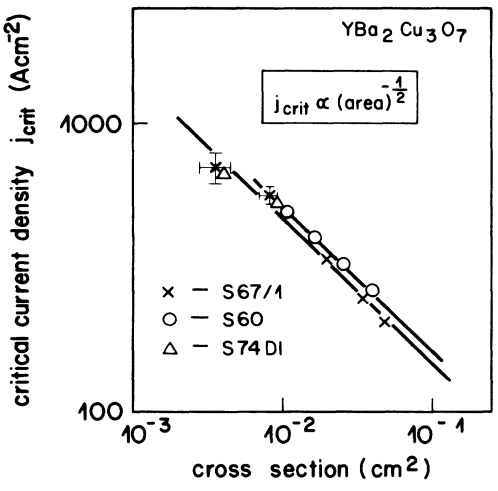

FIG. 4. Critical-current density as a function of the area of the constriction. Each curve represents one sample, the constriction being reduced after each measurement.

A more detailed model calculation will be presented in Sec. III. In the following paragraph, ac magnetization measurements are presented which directly confirm our hypothesis and which can be understood within the same framework.

B. ac magnetization

ac magnetization measurements at 77 K are used as an independent second routine material characterization. The usual pick-up coil assembly is used, i.e., the sample is placed inside a pick-up coil which, in turn, is situated in the homogeneous field of a larger solenoid. A sine-wave or triangular-shaped ac field is created by driving the outer solenoid with an appropriate power supply. The induced voltage in the pickup coil is monitored. For convenience, an identical, empty and adjustable pick-up coil is connected in series to compensate for induced signals without sample. By additionally connecting an integrator, we directly record the magnetization M as a function of the external magnetic field H_a. We should mention at that point that the actual H field within the sample is different (larger) from the applied field by an amount $-4\pi\mathcal{D}M$ where $\mathcal{D}$ is the demagnetization factor (~ 0.8). This effect will be most noticeable in the regime of large Meissner-Ochsenfeld effect (i.e., low fields). In the following figures no correction for demagnetization is done, i.e., we always use the external field strength H_a far from the sample. The ac frequency is chosen to be 20 Hz. Frequency-dependent measurements reveal only slight changes in signal shape (within 10%) between 1 and 500 Hz. The amplitude of the applied field can be varied be-

tween 0 and 1000 Oe.

Depending on the amplitude of the applied field the M vs H_a hysteresis loop displays different shapes which can be divided into four regimes. Typical results for the ceramic sample are illustrated in the left part of Fig. 5. Each sample shows qualitatively similar shapes, the details, however, may vary as will be discussed later in this section. At very small fields (≤ 1 Oe) all samples display Meissner shielding, i.e., the $4\pi M$ vs H_a curve is a straight line. This is depicted in Fig. 5(a). Only very bad samples (i.e., $j_{crit} < 50$ A cm^{-2}) exhibit hysteretic behavior but will also expel the flux at even lower external fields. Figure 5(b) shows the magnetization at a field of ~ 20 Oe. All samples display pronounced hysteretic behavior with flux penetrating the samples and remaining trapped at zero external field. Interestingly, the loop closes again at higher fields and goes over into a straight line with smaller slope compared to complete Meissner shielding. This reduced diamagnetic behavior is attributed to the diamagnetism of the disconnected grains. At even higher fields [Fig. 5(c)] the loop opens up again and more flux is able to penetrate the sample. Finally [Fig. 5(d)] the magnetization of the sample decreases strongly at fields above 200 Oe.

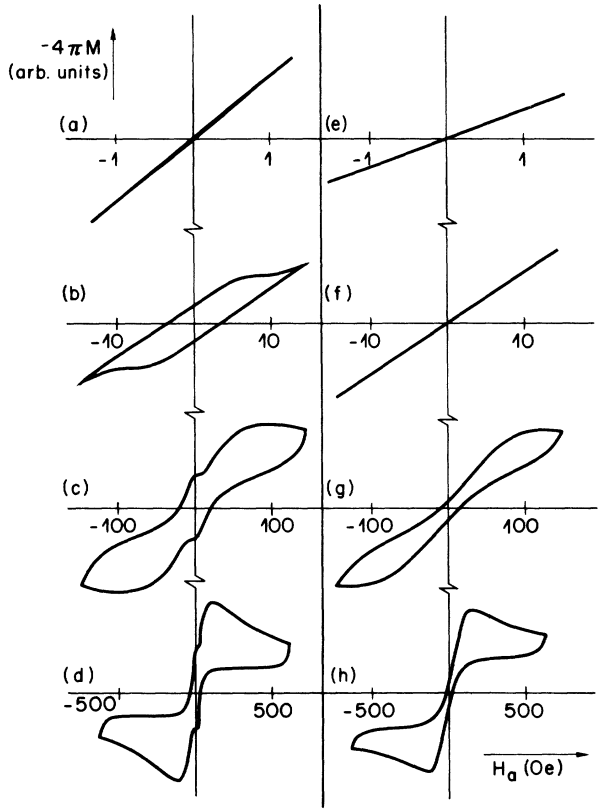

FIG. 5. (a)-(d) Magnetization versus applied magnetic field for the ceramic sample and for (e)-(h) the powdered sample. At low magnetic fields [≤ 1 Oe, (a)] the sample displays Meissner shielding. A first hysteresis loop opens as the field is increased beyond 1 Oe (b) and closes again at higher fields. The reversible behavior at elevated fields is attributed to the diamagnetism of the individual grains. As the external field is further increased (c) a second hysteresis loop opens which is attributed to the penetration of vortices into the grains themselves. Finally, the magnetic moment decreases strongly at high fields [> 200 Oe, (d)]. The powder sample shows only the second hysteresis loop (e)-(h).

The observed magnetization data show a behavior which is typical for granular superconductors. The different contributions of superconducting grains and intergrain couplings can be clearly distinguished. This becomes obvious and can be unambiguously demonstrated by grinding the sample into powder with a grain size smaller than 20 μm and embedding the powder in epoxy resin: The grinding destroys most of the intergrain connections but the bulk of the material is still present. Magnetization data for the powder sample are shown in Figs. 5(e)-5(h). It can be clearly seen that the hysteresis loop at low fields is absent while the high-field signal looks rather similar to the data for the ceramic sample. Obviously, the Meissner shielding and the hysteresis developing at low fields are due to the coupling of the grains while the signal at higher fields, which is present in both bulk and powdered materials, is due to grain properties.

In the following, we will concentrate on this two-step behavior and collect additional justification for dividing the sample into two subsystems, i.e., grains and grain connections. Figure 6 is a plot of the trapped magnetization [i.e., $-4\pi M(H_a = 0)$] as a function of the field amplitude of the loop. This can be visualized by taking a hysteresis loop of Fig. 5; the trapped flux is half the vertical opening in the middle whereas the field amplitude is given by half the horizontal width. This measurement can be considered sensitive to the magnetic field strength at which flux starts to penetrate the sample. Figure 6 shows that flux starts to penetrate at rather low fields. The regime of

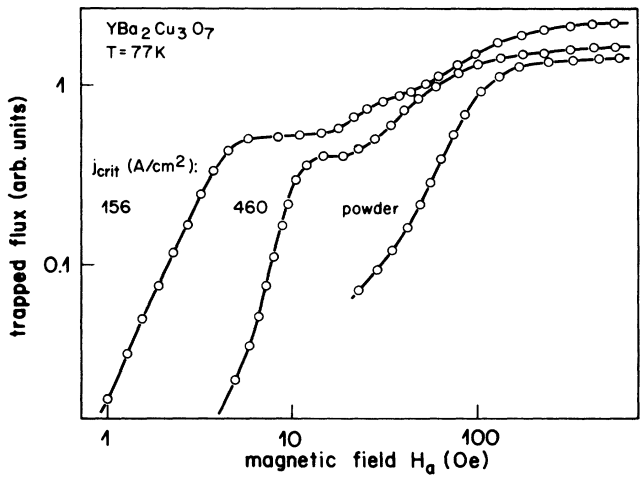

FIG. 6. Trapped magnetization [$-4\pi M(H_a = 0)$] as a function of the field amplitude of the loop. The regime of first penetration is attributed to flux trapping in the voids and between the grains and relies on the presence of intergrain currents. A reduction of the intergrain currents (lower j_{crit}) renders the sample weaker to the penetration of magnetic flux. The second rise of the trapped flux with increasing field amplitude is due to flux penetration into the grains themselves (vortices). In the powdered sample only the second penetration step is present.

first penetration saturates above ~10 Oe. At higher fields, a second penetration path becomes available and saturation does not occur below 1000 Oe. The powdered sample just exhibits the second penetration step. We conclude that in a first step flux penetrates through the grain boundaries and occupies the space in between grains and in cavities. We should mention that the magnetic field will also penetrate between the grains in the powdered sample. However, the flux will not be trapped there and thus will not show up as an additional source of hysteresis. The field at which penetration starts is a function of the coupling strength of the grains (see Sec. III) and we expect to see a correlation with the critical current. This correlation is indeed observed (Fig. 6): The first penetration of the lower-quality sample with a smaller j_{crit} takes place at a low magnetic field, where the high-j_{crit} sample still expels the magnetic field. The second rise in trapped flux occurs due to the penetration of the field into the individual grains. The associated lower critical field of the grains H_{c1} can be estimated using the magnetization data of Umezawa *et al.*:[18] At 77 K the lower critical fields [corrected for the temperature dependence of the Ginzburg-Landau parameter κ (Refs. 19 and 20)] are ~40 Oe for $H_{c1}^{\parallel}$ and ~260 Oe for $H_{c1}^{\perp}$. The value $H_{c1}^{\parallel}=(37\pm3)$ Oe has been quoted by Solin, Garcia, Vieira, and Hortal.[21] This value agrees reasonably well with the second upturn in trapped flux for the ceramic sample.

In the next experiment we measure the ac susceptibility as detected by a lock-in technique while varying the field amplitude. A typical curve is shown in Fig. 7. The result is reminiscent of experiments performed by Rosenblatt, Peyral, and Raboutou[15] on granular Nb superconductors and, more recently, on $YBa_2Cu_3O_7$.[2] Again, a two-step process is observed reflecting the flux penetration between and into the grains. We would like to point out two observations: (i) The penetration starts at higher fields than in published experiments.[2,15] Although this may partly be due to different experimental arrangements ($\chi=-1/4\pi$ means maximum signal in our setup, whereas it means minimum signal in Refs. 1 and 2) we think that our samples do in fact exhibit higher resistance to flux penetration. (ii) The penetration into the grains starts at rather low fields (<40 Oe). Both observations together show that the coupling between the grains is, in fact, rather strong: Typically, the critical-current density between the grains is reduced only by a factor of 10^2 as compared to the intragrain current density.

The present samples, however, are still limited by grain boundary effects. Therefore, the magnetization signal due to grain connections should be related to the critical current density of the samples. In deducing a meaningful quantity from the magnetization loop to correlate with j_{crit}, we notice that we have to avoid any quantity that depends on the amount of trapped flux which turns out to be completely unrelated to j_{crit}. This can be easily understood by considering the role of a few cavities and voids which will effectively increase the trapped flux without affecting the critical current or even decreasing it. On the other hand, we expect that the magnetization due to intergrain currents disappears simultaneously with the suppression of the critical current by a magnetic field, suggesting that the horizontal width of the inner hysteresis loop should correlate with the critical current density in the sample. We therefore define the "critical" magnetic field H_a^* as half the horizontal width of the inner hysteresis loop. To be more specific, we choose H_a^* at the intersection of the tangent in the point of inflection with the straight line describing the reduced diamagnetic behavior of the disconnected grains (see inset in Fig. 8). This quantity will give the horizontal extension of the hysteresis loop without being affected by either the amount of trapped flux nor the grain diamagnetism. For a number

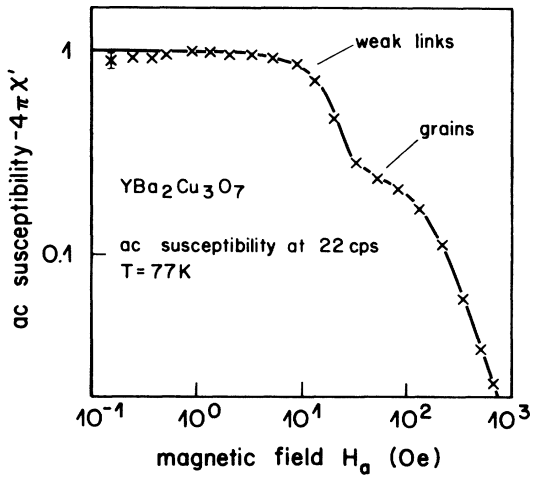

FIG. 7 ac susceptibility vs magnetic field amplitude. The magnetic field starts to penetrate into the sample at a field of $\simeq 1$ Oe. From this we estimate the penetration depth into the ceramic $\lambda_{cer}\simeq 2$ μm and the maximal intergrain current density to be of the order of 10^3 A cm^{-2}. Again the penetration of the ceramic can be clearly distinguished from the penetration of flux into the grains.

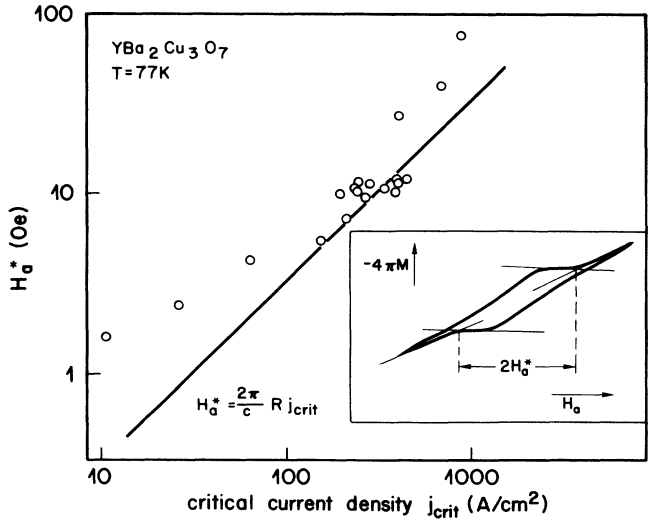

FIG. 8. Critical field H_a^* vs critical-current density. The linear relationship can be understood on the basis of the self-field limitation of the critical-current density in the ceramic sample; see Eq. (3). The inset illustrates the determination of H_a^*.

of samples we have plotted this quantity as a function of the critical-current density determined by the resistive technique described above (see Fig. 8). A linear relationship is observed over nearly two decades, indicating a very close relationship between the two quantities. In fact, other properties of the magnetization loop (i.e., Meissner shielding, trapped flux, maximum magnetic moment, field at maximum moment, etc.) are found to show no or very weak correlation with the critical current.

The relation between $j_{\rm crit}$ and H_a^* can be understood qualitatively by considering the simple model which we discussed in Sec. II A. Assuming that the decrease of the magnetization at H_a^* is due to the destruction of the shielding currents by the magnetic field, we can, to a first approximation, identify H_a^* and B^* in the local j_c vs B relation [Eq. (1)]. Since we found earlier that $j_{\rm crit}$ is completely determined by B^*, we can calculate B^* (or H_a^*) using $j_{\rm crit}$ and the known constriction radius R according to the formula

$$H_a^* = \frac{2\pi}{c} j_{\rm crit} R \,. \tag{3}$$

This quantity is also plotted in Fig. 8. Surprisingly good agreement between the experimental data and the prediction of Eq. (3) is found, relating data from a transport experiment with a measurement of the magnetization. We would like to emphasize that no adjustment of the data is performed at any point in the analysis and that the curve represents a true zero-parameter fit. Demagnetization effects and corrections due to the grain diamagnetism will only slightly modify this result as will be discussed in Sec. III.

Such a behavior is not observed in conventional superconductors and requires a careful reinterpretation of many experimental results obtained on oxide superconductors. Contrary to conventional superconductivity, the macroscopic $j_{\rm crit}$ is no real material property but is rather determined by H_a^* via a geometry factor. The true local j_0 which can be considered a material property is still unknown at present, but certainly well above 1000 A cm^{-2} in the best ceramics. On the other hand, we expect H_a^* to be a universal and size-independent quantity which actually characterizes the material and which can be easily determined.

At this point, we have established that the macroscopic critical currents and magnetization can be traced to a local j_c vs B relation, where j_c decreases steeply on a scale H_a^*. H_a^* is the most relevant quantity for the present materials and geometries. The experimental results can be understood on a semiquantitative basis using the simple step function approach [Eq. (1)]. In the following, we will deduce and outline a quantitative model which can be used for modeling and calculating actual sample (and device) properties. For a given geometry and j_c vs B relation, an analytical solution is derived and compared with experimental results.

III. CRITICAL STATE MODEL

We start with a discussion of the magnetic properties of a granular superconductor which is characterized by the diamagnetic behavior of the grains and a strong magnetic-field dependence of the critical-current density limiting the transport between the grains. The magnetization and transport properties are then calculated using a specific model for the critical-current density $j_c(B)$.

A. Granular superconductors

We consider a granular material with weakly coupled superconducting grains of mean size a. The coupling energy is $E_J = (\Phi_0/2\pi c) I_J$ where $\Phi_0 = hc/2e$ is the flux unit and I_J is the maximal Josephson current flowing between adjacent grains. The grains themselves are considered superconducting with a condensation energy $E_g = H_{cg}^2 a^3/8\pi$ which is much larger than the coupling energy E_J between the grains. (H_{cg} is the thermodynamic critical field of the grains.) In this limit, which applies well to the oxide superconductors, the current in the ceramic is limited by the coupling E_J and not by the suppression of the order parameter in the grains.[4]

Applying a magnetic field to such a granular superconductor has two effects: First, the grains themselves behave as diamagnets, expelling the field from their interior. Second, Josephson currents flowing between the grains lead to the expulsion of flux from the interior of the ceramic sample.

Let us first consider a sample with zero coupling between the grains. Assuming a fraction f_n of the volume to be permeable ($\mu = 1$) and the remaining fraction $f_s = 1 - f_n$ to be superconducting, we can characterize the magnetic response of the sample by the effective permeability of the ceramic, $\mu_{\rm cer} = f_n + f_s \mu_g$. Here μ_g is the effective permeability of the superconducting grains defined by $\mu_g = \Phi_s/\Phi_n$, Φ_s and Φ_n being the flux penetrating into the grain under superconducting and normal conditions, respectively. The magnetic field B inside the sample is then approximated by the average $\langle b \rangle = \mu_{\rm cer} H$ of the microscopic field b taken over a volume which is large compared to the average grain size. Here H is the external applied field. Assuming a cylindrical shape for the individual grains the permeability μ_g becomes

$$\mu_g = \frac{4\lambda}{a} \frac{I_1(a/2\lambda)}{I_0(a/2\lambda)} \,.$$

a and λ denote the size and the penetration depth of the grains, respectively, and I_n is the modified Bessel function.[22] For our best ceramic samples the grain size a lies in the range 1–10 μm and at 77 K the mean penetration depth λ is estimated to be ~ 1 μm.[23] With a superconducting fraction $f_s = 0.95$ we obtain an effective permeability $\mu_{\rm cer} \simeq 0.5$ for our ceramics. The expected magnetic response then is given by a reduced diamagnetic behavior $-4\pi M = (1 - \mu_{\rm cer}) H$.

As the coupling E_J between the grains is turned on, coherence between the grains is established and screening currents start to flow through the sample. In the following we will briefly derive the phenomenology of a ceramic superconductor. This discussion will lead us to a modified critical state model which describes well the magnetic and transport properties of the ceramic samples.

The free-energy density of the coherent state is given by the expression

$$f_c(T,B)=e_g(T)+e_m(B)+e_c(T,B)\,.$$

$e_g(T)$ denotes the condensation energy density of the grains and $e_m(B)=B^2/8\pi\mu_{cer}$ is the magnetic energy density of the uncoupled superconducting sample.[24] A simple approximation for the coupling energy density is

$$e_c(T,B)=\frac{E_J}{a^3}\left\{1-\cos\left[\mathbf{a}\left[\nabla\phi-\frac{2\pi}{\Phi_0}\mathbf{A}\right]\right]\right\}, \qquad (4)$$

where ϕ is the phase of the superconducting order parameter and $\mathbf{a}$ is the vector connecting two adjacent grains. Equation (4) applies to the situation where the current enters and leaves the grain through a single adjacent grain, respectively. The temperature dependence of e_c arises from the temperature dependence of the coupling E_J.

The vector potential $\mathbf{A}$ generates the total induction

$$\nabla\times\mathbf{A}=\mathbf{B}=\mathbf{H}+4\pi\mathbf{M}_g+4\pi\mathbf{M}_J\,, \qquad (5)$$

which is due to the external field $\mathbf{H}$, the screening currents flowing in the grains generating $\mathbf{M}_g$, and the Josephson screening currents flowing through the whole sample and generating $\mathbf{M}_J$. The magnetization $\mathbf{M}_g$ depends on the total field applied to the grains which is $\mathbf{H}+4\pi\mathbf{M}_J$, thus

$$\mathbf{M}_g=\chi_{cer}(\mathbf{H}+4\pi\mathbf{M}_J),\quad \mu_{cer}=1+4\pi\chi_{cer}\,. \qquad (6)$$

The magnetization $\mathbf{M}_J$ is generated by the Josephson currents $\mathbf{j}_J$,

$$\nabla\times\mathbf{M}_J=\frac{1}{c}\mathbf{j}_J\,,$$

and therefore, using (5) and (6), we obtain

$$\nabla\times\mathbf{B}=\frac{4\pi}{c}\mu_{cer}\mathbf{j}_J\,,$$

telling us that the magnetization due to the Josephson currents is reduced ($\mu_{cer}<1$) by the diamagnetism of the grains.

The second equation relating the Josephson current density $\mathbf{j}_J$ and the magnetic field is found by minimizing the free energy of the coherent state with respect to $\mathbf{A}$,

$$\nabla\times\nabla\times\mathbf{A}=\frac{4\pi}{c}\mu_{cer}\frac{I_J}{a^2}\hat{\Phi}\sin(\mathbf{a}\cdot\mathbf{\Phi})\,,$$

$$\mathbf{\Phi}=\nabla\phi-\frac{2\pi}{\Phi_0}\mathbf{A}\,.$$

In the expression for the Josephson current density $\mathbf{j}_J$ the permeability μ_{cer} drops out

$$\mathbf{j}_J=\frac{I_J}{a^2}\hat{\Phi}\sin(\mathbf{a}\cdot\mathbf{\Phi})\,.$$

This is not the case, however, for the penetration depth λ_{cer} of the ceramic: Applying twice the curl on the gauge-invariant phase gradient $\mathbf{\Phi}$ we obtain (in the absence of vortices)

$$\Delta\mathbf{\Phi}=\frac{8\pi^2\mu_{cer}I_J}{ca^2\Phi_0}\hat{\Phi}\sin(\mathbf{a}\cdot\mathbf{\Phi}) \qquad (7)$$

and, therefore, a London penetration depth

$$\lambda_{cer}=\left(\frac{ca\Phi_0}{8\pi^2\mu_{cer}I_J}\right)^{1/2}\,.$$

The penetration depth *increases* with increasing quality ($\mu_{cer}\rightarrow 0$) of the material. This result can be understood in the following way (see Fig. 9): The Josephson current $\mathbf{j}_J$ generates a field $1/c\nabla\times\mathbf{j}_J$ opposing the external field $\mathbf{H}$. The diamagnetic currents in the grains then consist of two contributions; a first contribution shields the interior of the ceramic from the applied external field and therefore supports $\mathbf{j}_J$. This current flows within a depth λ from the sample surface. A second contribution to $\mathbf{M}_g$ arises from the diamagnetic field $\mathbf{M}_J$ which induces currents in the grains *opposing* M_J. The net effect is a reduction of the external field H to $\mu_{cer}H$ and a reduction of the screening current $\mathbf{j}_J$ by a term $(1-\mu_{cer})\mathbf{j}_J$ due to the diamagnetic grains. As a consequence, the magnetic field penetrates a longer distance into the sample, explaining the rise of λ_{cer} as $\mu_{cer}\rightarrow 0$.

The critical field H_c^* of the ceramic is the largest field which can be screened to zero asymptotically. The Josephson currents have to screen the remaining field $\mu_{cer}H$ since a fraction $(1-\mu_{cer})H$ is screened by the diamagnetism of the grains (see Fig. 9). Using Eq. (7), the

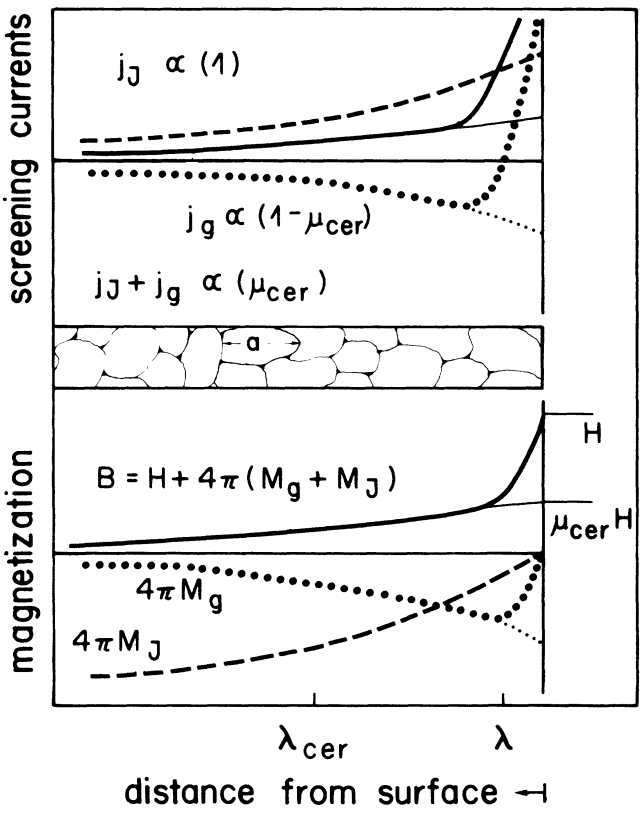

FIG. 9. Screening currents and magnetization vs position near the surface of a granular superconductor. The combined effects of intragrain (dotted line) and intergrain (dashed line) screening currents lead to a rapid decay of the external field H to $\mu_{cer}H$ within a length λ followed by a smoother decay to zero on the scale λ_{cer}.

result for H_c^* is

$$H_c^* = \frac{\Phi_0}{\pi \mu_{cer} \lambda_{cer} a} .$$

With increasing quality of the ceramic ($\mu_{cer} \to 0$) the critical field H_c^* and λ_{cer} simultaneously increase, showing that the diamagnetic screening of the sample is more and more due to the grain diamagnetism.

For our ceramic oxide superconductors, we estimate a maximal intergrain current density of the order of $j_J = I_J/a^2 \simeq 10^3$ A cm^{-2}, resulting in a penetration depth λ_{cer} which is of the order of the grain size a ($\lambda_{cer} \simeq 1-5$ μm). The critical field H_c^* is a few oersteds. For the case of $\lambda_{cer} > a$ intergranular vortices will penetrate the sample at the lower critical field $H_{c1}^* \simeq \Phi_0/4\pi\mu_{cer}\lambda_{cer}^2$ which is about 1 Oe in our samples. This estimate agrees well with the field of first flux penetration found experimentally (see Figs. 6 and 7). On the other hand, for large grain size $a > \lambda_{cer}$ the field penetrates into the sample in the form of Josephson vortices[6] which are characterized by the length scale $\lambda_J = (c\Phi_0/8\pi^2 j_J d)^{1/2}$. Here $d = 2\lambda + \omega$ is the total penetration depth of the field into the junction and the adjacent grains, ω being the width of the junction. When discussing the permeability we have used an average value of the anisotropic penetration depth λ. For the intergrain transport properties, we consider the good junctions resulting from grains with their CuO planes parallel to the junction normal. The relevant penetration depth $\lambda^{\perp}$ then is of the order of 0.2 μm at 77 K.[18,25,26] Neglecting the width ω of the junction, we obtain a Josephson penetration depth $\lambda_J \simeq 5$–10 μm and a lower critical field $H_{c1}^J = 2\Phi_0/\pi^2\lambda_J d$ again of the order of 1 Oe. Thus, for the case of large grains the role of intergrain vortices is taken over by the Josephson vortices. Note that in both cases of small and large grains it is essential to distinguish between two types of vortices in the ceramic material: intragrain vortices which are based on the large intragrain current densities, and intergrain or Josephson vortices which rely on the reduced intergrain current densities j_J. The two different scales of current densities present in the ceramic material constitute the basis for the observed transport and magnetic properties.

The above discussion shows that the ceramic material will essentially behave like a type-II superconductor where the current and the magnetic field penetrate the whole sample. This allows us to model the transport and magnetic properties of the ceramic sample using a critical-state model which assumes that the current density in the sample is always at its critical value. Contrary to Bean's original model[7] it is important to take the strong dependence of the critical-current density on the magnetic field B into account. This strong dependence on B is observed experimentally and can be understood theoretically on the basis of the strong magnetic-field dependence of the grain coupling typical for Josephson junctions.

In the following, we calculate the ac magnetization and the effective critical current within the critical-state model. The microscopic current-field relation is approximated by

$$j_c(B) = j_0 \left[1 - \frac{|B|}{B^*} \right] \Theta(B^* - |B|) , \tag{8}$$

where B is the local magnetic induction and $\Theta(x)$ denotes the Heaviside step function. This model for $j_c(B)$ describes well the sharp drop of the critical current on a scale of ~ 100 Oe found experimentally. The tail extending to higher fields (> 100 Oe) is neglected within this approximation.

B. Magnetization

The magnetization M of the sample is given by

$$4\pi \mathbf{M} = \frac{1}{V} \int d^3x [\mathbf{B}(\mathbf{x}) - \mathbf{H}] ,$$

with $\mathbf{B}(\mathbf{x})$ and $\mathbf{H}$ denoting the local induction and the external magnetic field, respectively (we will discuss demagnetization effects later). The induction $\mathbf{B}(\mathbf{x})$ is determined by Maxwell's equation

$$\nabla \times \mathbf{B} = \frac{4\pi\mu_{cer}}{c} j_c(B) .$$

For a cylindrical sample (with the axis parallel to z and radius R) these equations reduce to $\{\mathbf{B}(\mathbf{x}) = [0,0,B(r)]\}$

$$4\pi M = \frac{2}{R^2} \int_0^R dr\, r [B(r) - H] , \tag{9}$$

and

$$\frac{dB}{dr} = \pm \frac{4\pi\mu_{cer}}{c} j_0 \left[1 - \frac{|B|}{B^*} \right] . \tag{10}$$

Here the + (−) sign applies to screening currents induced by rising (decreasing) external fields H. The boundary condition which fixes the solution of Eq. (10) is

$$B(R) = \mu_{cer} H , \tag{11}$$

i.e., only the remaining fraction $\mu_{cer}H$ has to be screened by the Josephson currents, the rest being screened by the diamagnetic grains as discussed above. The calculation of the magnetic hysteresis $M(H)$ is somewhat tedious because of the memory effects. As an example, we consider here only the simplest case of a zero-field-cooled sample in a rising external field, deferring the full description of the hysteresis to the Appendix.

The solution of Eq. (10) subject to the boundary condition (11) is

$$B(r) = \begin{cases} 0, & 0 < r < r_m , \\ B^*(1 - e^{\alpha(R-r)}) + \mu_{cer} H e^{\alpha(R-r)}, & r_m < r < R , \end{cases}$$

with (see Fig. 10)

$$R - r_m = \begin{cases} \dfrac{1}{\alpha} \ln \dfrac{B^*}{B^* - \mu_{cer} H}, & 0 < H < \dfrac{B^*}{\mu_{cer}} (1 - e^{-\alpha R}) , \\ R, & \dfrac{B^*}{\mu_{cer}} (1 - e^{-\alpha R}) < H < \dfrac{B^*}{\mu_{cer}} . \end{cases} \tag{12}$$

Here we have set H_{c1}^* equal to zero, the corrections due to a finite value being small ($\mu_{cer} H_{c1}^* \ll B^*$). B^* is the maximal local field which can be screened by the Josephson currents [see Eq. (8)] and the parameter $1/\alpha = cB^*/$

$4\pi\mu_{cer}j_0$ determines the length scale on which the Josephson screening currents flow. Averaging the induction over the volume of the cylinder [Eq. (9)] we find

$$\langle B\rangle = \begin{cases} B^*\left[1-\dfrac{r_m^2}{R^2}\right]-\dfrac{2}{(\alpha R)^2}(B^*-\mu_{cer}H)[(1+\alpha r_m)e^{\alpha(R-r_m)}-(1+\alpha R)], & 0<H<\dfrac{B^*}{\mu_{cer}}, \\ \mu_{cer}H, \quad \dfrac{B^*}{\mu_{cer}}<H. \end{cases} \tag{13}$$

From this result, we immediately obtain the magnetization $M(H)$ using Eq. (9). The result for a field $H<0$ applied to a virgin sample is obtained by substituting $-B^*$ for B^* in the above formulas.

The above derivation applies to the case of a virgin sample in a rising external field H. Assume the field is reversed at a value $H_m<B^*/\mu_{cer}$. For all field values $|H|<H_m$ the sample will remember this maximal field: with decreasing external field H the screening currents are gradually reversed. In Fig. 10 a situation is shown where the external field H was reversed after reaching a maximum H_m. As a consequence the screening currents have been reversed up to a depth $R-r_i$ from the sample surface. Obviously, these screening currents differ a lot from the case of a virgin sample subject to the same external field H. This memory effect leads to the magnetic hysteresis loop for fields $|H|<B^*/\mu_{cer}$. Such a hysteresis loop is shown in Fig. 11 (no demagnetization effects are taken into account here, therefore $H=H_a$). The arrows mark the fields H_m and H used in Fig. 10 and illustrate how the external field initially penetrates the sample very slowly. Only as H approaches the maximal field B^*/μ_{cer} very closely does the field penetrate rapidly towards the center of the sample [see also Eq. (12)], leading to the steep decrease of the magnetization as $H\rightarrow B^*/\mu_{cer}$. For fields $|H|>B^*/\mu_{cer}$ no Josephson screening currents can circulate in the cylinder and the sample behaves reversible and diamagnetic.

We briefly discuss the hysteresis loop resulting for the truncated Bean model characterized by Eq. (1): Instead of a continuous transition to the reversible diamagnetic behavior $-4\pi M=(1-\mu_{cer})H$, the truncated Bean model leads to a discontinuity of $M(H)$ at $|H|=B^*/\mu_{cer}$. Whereas the Josephson screening currents decay continuously as $|H|$ approaches B^*/μ_{cer} in the above model, the screening currents collapse from their value j_0 to zero for the model of Eq. (1). The discontinuity in the hysteresis loop is removed by introducing a smooth decay in the current-field relation $j_c(B)$. A sharp drop in the $M(H)$ relation will remain, however, indicating the sharp drop in $j_c(B)$ at the corresponding field $B=\mu_{cer}H$. A further difficulty, apart from the discontinuity in $M(H)$, is the ambiguity in fitting an experimental $j_{crit}(H_a)$ relation with Eq. (1): an "equal area" fit and a fit of j_0 and H_a^* ("double area") will lead to very different hysteresis loops, neither of which fit the experimental data well. We thus conclude that the truncated Bean model is less appropriate for an accurate analysis of the magnetization

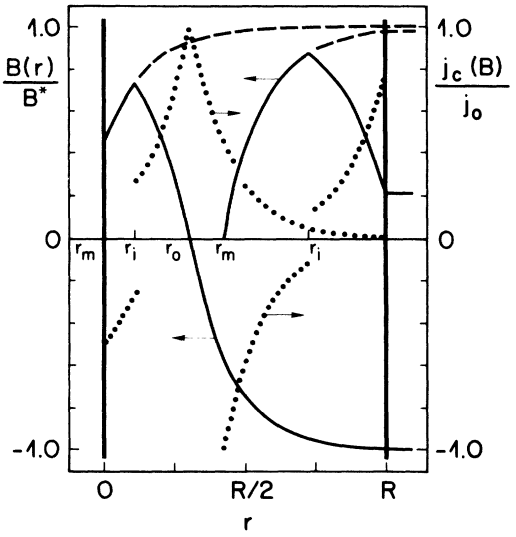

FIG. 10. Screening currents and magnetic induction as a function of position for a linear current-field relation $j_c(B)$. The parameters used are $j_0=650$ A cm^{-2}, $B^*=22.5$ G, and $R=0.4$ cm. The Josephson currents decay on a length scale $1/\alpha=0.057$ cm. The external field H was first increased to $H_m=46$ (46.85) Oe and reduced afterwards to $H=10$ (-46.5) Oe. For $H_m=46.85$ Oe the field has penetrated to the center of the sample ($r_m=0$). The radii r_i and r_0 denote the positions of current reversal and maximal screening current, respectively.

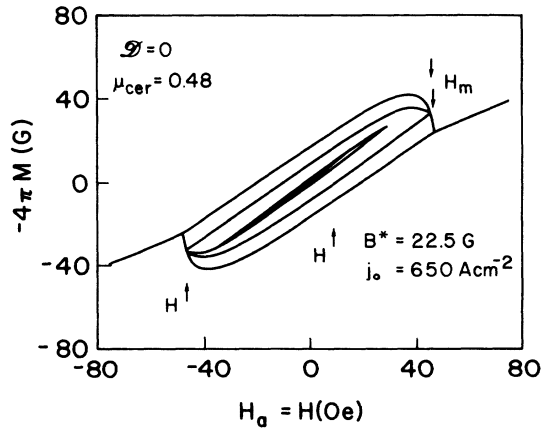

FIG. 11. Magnetic hysteresis loop without demagnetization effects. The external field $H=H_a$ is alternately increased and decreased, reversing the field at $H_a=\pm 2.5$, ± 7.6, ± 15, ± 23, ± 30, ± 45, ± 61, and ± 76 Oe. The hysteresis loop closes at a value $H=B^*/\mu_{cer}=46.88$ Oe. The arrows indicate the applied fields H_m and H used in Fig. 10 for the illustration of the screening currents and the magnetic induction.

data.

Before we can compare our model calculations with experimental results we have to discuss demagnetization effects. For a sample in the form of an ellipsoid of revolution (with d and R the lengths of the semiaxis) the magnetic field H and the applied asymptotic field H_a are related by the equation[19]

$$H = H_a - 4\pi \mathcal{D} M = H_a - \mathcal{D}(B - H) . \tag{14}$$

The samples used in our experiments are flat disks of radius $R \simeq 0.6$ cm and height $2d \simeq 0.1$ cm, implying a demagnetization coefficient $\mathcal{D} = 1 - (\pi/2)d/R \simeq 0.85$. Substituting B in Eq. (14) by $\langle B \rangle$ [Eq. (13)] we obtain an implicit equation for H. The quantities H, $\langle B \rangle$, and $4\pi M$ must therefore be calculated self-consistently for each value of the applied field H_a. Figure 12 shows the magnetic hysteresis loop calculated with the same parameters as used in Fig. 11 before, but including demagnetization effects. The actual internal field H is enhanced over the applied field H_a, leading to the narrowing of the hysteresis loop. Again we have marked the fields H_a and H_{ma} corresponding to the field and current patterns of Fig. 10. The demagnetization effects lead to a spreading of the regime where the external field sweeps rapidly into the sample.

Particularly simple are the two limits $H \to 0$ and $H > B^*/\mu_{cer}$:

$$-4\pi M = \begin{cases} \dfrac{H_a}{1-\mathcal{D}}, & H < H_{c1}^* , \\ \dfrac{(1-\mu_{cer})H_a}{1-(1-\mu_{cer})\mathcal{D}}, & H > \dfrac{B^*}{\mu_{cer}} . \end{cases}$$

An analysis of the two slopes of $M(H_a)$ at low and high values of H_a provides additional information $(\mathcal{D}, \mu_{cer})$ on the ceramic sample. The hysteresis loop closes at a value

$$H_a^* = \frac{1-(1-\mu_{cer})\mathcal{D}}{\mu_{cer}} B^* . \tag{15}$$

Solving for B^*, the magnetization data can be used to determine the parameter B^* in the local current-field relation $j_c(B)$.

Finally, we compare our model calculations with experimental results. In Fig. 13 we show a magnetic hysteresis

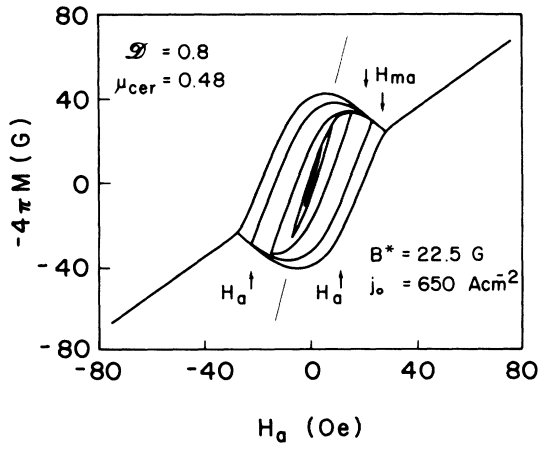

FIG. 12. Magnetic hysteresis loop based on a self-consistent calculation of H, $\langle B \rangle$, and M, including demagnetization effects. The same parameters as for Fig. 11 are used. The demagnetization enhances the internal field H, leading to a narrowing of the hysteresis loop. Again the arrows mark the applied fields H_m and H used in Fig. 10.

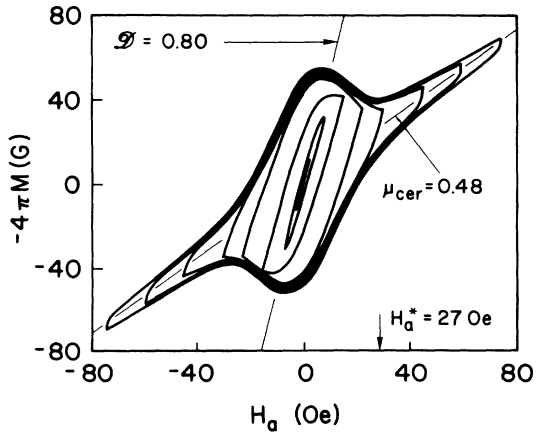

FIG. 13. Magnetic hysteresis loop measured on a sample of radius $R = 0.59$ cm and thickness $2d = 0.1$ cm. The critical current through a constriction of 0.01 cm^2 is 420 A cm^{-2}. The external field H_a is gradually increased up to 76 Oe with field reversals as in Figs. 11 and 12. From the slopes at low and high fields one finds $\mathcal{D} = 0.8$ and $\mu_{cer} = 0.48$, respectively. The "critical" magnetic field is $H_a^* \simeq 27$ Oe from which we deduce $B^* = 22.5$ G. The wings at large values of $|H_a|$ (> 27 Oe) are due to the finite tail in the current-field relation $j_c(B)$.

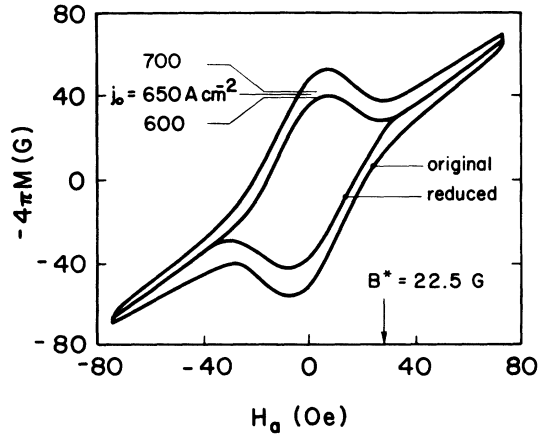

FIG. 14. Magnetic hysteresis loop before and after the subtraction of the wings at high fields $|H_a| > 27$ Oe. The subtraction is done by linear extrapolation of the high field data to lower fields. The result is compared to model calculations and a value $j_0 = 650$ A cm^{-2} is found to reproduce well the data. The whole magnetization loop is then calculated with the parameters found from the analysis of Figs. 13 and 14 and the result is shown in Fig. 12.

loop where the external field has been alternately increased and decreased up to $H_a = 76$ Oe with field reversals at $H_a = \pm 2.5$, ± 7.6, ± 15, ± 23, ± 30, ± 45, ± 61, and ± 76 Oe. From the two slopes at $H < H_{c1}^*$ and $H > B^*/\mu_{cer}$ we find a demagnetization factor $\mathcal{D} = 0.80$ and a permeability $\mu_{cer} = 0.48$, respectively. The expected value for the demagnetization factor is 0.81. This value has been calculated for the sample with a constriction as shown in Fig. 1 by using a radius corresponding to a disk with half the sample area. The sample radius is $R = 0.59$ cm and the effective radius becomes $R_{eff} = 0.42$ cm. The thickness of the cylinder is 0.1 cm. The magnetization shows a local minimum at $H_a^* = 27.0$ Oe. This value is converted to a critical field $B^* = 22.5$ G using Eq. (15). The last parameter to determine is j_0. In our simplified model, we neglect the tail at large fields in the current-field relation $j_c(B)$. This tail contributes to the magnetization and leads to the narrow wings in the magnetization loop at fields $|H_a| > H_a^*$. In order to obtain a correct value for j_0, we first have to subtract this contribution from our data. Figure 14 shows the experimental data before and after subtraction of the wings (only the maximal open loop is shown). The parameter j_0 is found by a comparison of the loop height with model calculations. A value $j_0 = 650(\pm 50)$ A cm^{-2} agrees well with the experimental results. The dependence of the hysteresis loop on j_0 is, however, much weaker than the dependence on B^*, showing again that large samples of dimension $> 1/\alpha$ are characterized by B^* rather than the maximal critical current j_0. Finally the whole hysteresis loop with the gradually increased field is shown in Fig. 12. All the structure and the size of the loops are well reproduced by the model calculation.

C. Critical current

The effective critical current density j_{crit} carried by a wire of cylindrical shape (radius R) can be calculated along the same lines. Using again the linear current-field relation Eq. (8) we have to solve the differential equation $[\mathbf{B}(\mathbf{x}) = B(r)\mathbf{e}_\phi]$

$$\frac{d}{dr}[rB(r)] = \frac{4\pi\mu_{cer}}{c} r j_0 \left[1 - \frac{B}{B^*}\right],$$

with the boundary condition $B(r=0) = 0$. The magnetic induction $B(r)$ is limited by B^*,

$$B(r) = B^* \left[1 - \frac{1}{\alpha r}(1 - e^{-\alpha r})\right] < B^*,$$

such that the total current I_{crit} carried by the wire grows only linearly in R as the radius becomes large, $\alpha R \gg 1$:

$$I_{crit}(R) = \frac{cR}{2\mu_{cer}} B(R).$$

The apparent critical current density then is

$$j_{crit} = \frac{I_{crit}}{\pi R^2} = j_0 \frac{2}{\alpha R}\left[1 - \frac{1}{\alpha R}(1 - e^{-\alpha R})\right]$$

$$= \begin{cases} j_0\left[1 - \dfrac{\alpha R}{3}\right], & R \to 0, \\ j_0 \dfrac{2}{\alpha R} = \dfrac{cB^*}{2\pi\mu_{cer} R}, & R \to \infty. \end{cases}$$

Using Eq. (15), we recover Eq. (3) up to a factor $1 - (1 - \mu_{cer})\mathcal{D}$ which introduces a correcting factor $\simeq 0.6$ in Eq. (3). The self-limitation of the critical current by the magnetic field becomes effective at a radius $R \simeq 1/\alpha$ which is 0.057 cm in our test sample with $j_0 = 650$ A cm^{-2} and $B^* = 22.5$ Oe. Using the above formula to calculate the expected current density through the constriction in the sample (area $\simeq 0.01$ cm^2, see Fig. 1), we obtain a value $j_{crit} = 480(\pm 30)$ A cm^{-2}. This compares reasonably well with the measured value $j_{crit} = 420$ A cm^{-2}.

The same calculation can be done for a (thin) film and the result is

$$j_{crit} = j_0 \frac{2}{\alpha d}(1 - e^{-\alpha d/2}),$$

where d is the film thickness. With the parameters deduced above thin films of thickness less than 100 μm do not suffer from self-field limitation.

We note that the self-limitation effects depend on the local current-field relation $j_c(B)$. To provide an idea for this dependence we quote our results for the case of the smoothly decaying Anderson-Kim[27,28] relation

$$j_c(B) = \frac{j_0}{1 + B/B^*}. \tag{16}$$

The current j_c initially decays with a slope $-j_0/B^*$ in both expressions Eq. (8) and (16), however, an additional tail is present in Eq. (16) at high fields $B > B^*$. Due to this tail the magnetic field is no longer limited to values $B < B^*$ and the critical-current density decays only with the square root of the sample diameter:

$$j_{crit} \sim \begin{cases} j_0\left[\dfrac{8}{3}\dfrac{1}{\alpha R}\right]^{1/2}, & R \gg \dfrac{1}{\alpha}, \text{ cylindrical wire}, \\ j_0\left[\dfrac{4}{\alpha d}\right]^{1/2}, & d \gg \dfrac{1}{\alpha}, \text{ thin film}. \end{cases}$$

IV. SUMMARY AND DISCUSSION

In this paper, we have presented experimental results demonstrating that the transport and magnetic properties of bulk ceramic high-T_c superconductors are dominated by the strong dependence of the local current density on the magnetic field. Based on a local current-field relation which decays on the scale of a critical field B^*, we could

explain the decay of the critical current density $j_{crit} \sim B^*/R$ with increasing radius R of the macroscopic wire. Furthermore, the critical current scales with the critical field B^* at large radii and only for very thin wires (at least $R < 0.05$ cm for the present material) one can expect to observe the maximal current density j_0.

The magnetization of the ceramic sample is characterized by two field scales: For applied fields $H_a < H_a^*$ a first hysteresis loop opens which is due to the trapping of intergrain vortices in the ceramic sample. For intermediate fields $H_a^* < H_a < H_{c1}^{\parallel}$ the hysteresis loop closes and opens again at large fields $H_a > H_{c1}^{\parallel}$, where vortices start to enter the grains themselves. The inner and the outer hysteresis loop can be analyzed to obtain information on the granular superconductor and on the superconducting grains, respectively. We have presented a model calculation of the inner hysteresis loop based on an improved critical state model which takes the strong decay of the critical-current density with increasing magnetic induction into account. Accounting for the diamagnetism of the grains and for demagnetization effects by a self-consistent determination of the external field H_a, the internal magnetic field H, and the magnetic moment M, we could compare the theoretical results with the measured hysteresis loop. The analysis allows for the determination of the relevant microscopic parameters μ_{cer}, j_0, and B^*. The parameters obtained in this way from the magnetization data are compatible with the transport data, thus, giving us a consistent description of the granular superconductor.

Finally, we discuss the mechanism which possibly limits the critical-current density in the present ceramic material. Within the model presented above two mechanisms can put an upper limit on the current density: (i) depinning of intergrain vortices, and (ii) suppression of the effective grain coupling by the magnetic field. The pinning force for the intergrain vortices depends on the amount of disorder in the coupling strengths between the grains, however, nothing definite can be said about its actual size yet. First results on the pinning potential in a square array of identical Josephson junctions have been given by Lobb, Abraham, and Tinkham.[5] On the other hand, we can estimate the suppression of the grain coupling by the magnetic field: The average flux Φ penetrating a Josephson junction is $\Phi \simeq 2\lambda^{\perp} aB\pi/4\mu_{cer}$, where the factor $\pi/4$ is due to the average over the angle enclosed between the magnetic induction and the normal to the junction. The factor μ_{cer} enters the expression because the field within the junction is enhanced over the average field B in the ceramic. Here we use again the penetration depth $\lambda^{\perp} \simeq 0.2$ μm since we consider only the good junctions resulting from grains with their CuO planes parallel to the junction normal in the discussion of the transport properties. For the grain size we estimate $a \simeq 1$–5 μm. The sharp drop in the coupling constant will take place on a scale $\Phi^* = \Phi_0$ resulting in an estimate for the critical field B^* of the order of 10 G. This result agrees well with the critical field found in our analysis above. We thus conclude that the limiting factor for intergrain current transport in our samples are the Josephson junctions and not the intergrain vortex pinning force. In addition our analysis is consistent with Josephson junctions at the grain boundaries and not at the twinning boundaries, in agreement with results reported by Peterson and Ekin[29] and Kwak, Venturini, Nigrey, and Ginley.[30]

Note added. In Fig. 1, the differential resistance at high bias does not increase with increasing external field H_a. The field-independent differential resistance can then be interpreted as the normal junction resistance. On the other hand, a linear increase of the differential resistance with increasing applied field H_a is expected for a critical current limited by vortex depinning[31] (flux-flow resistance). This gives additional support for our conclusion that the intergrain current transport in our samples is limited by the Josephson junctions. We thank J. Rhyner for pointing this observation out to us.

ACKNOWLEDGMENT

We wish to thank R. Marsolais, J. Rhyner, and H. J. Wiesmann for helpful discussions and appreciate the technical assistance of P. Unternährer, R. Weder, and R. Krieg. Part of this work was supported by the Swiss National Science Foundation.

APPENDIX

In this appendix, we calculate the full hysteresis loop $M(H)$ for the situation where the magnetic field H is varied between the extremes $-H_m$ and H_m. We have to determine the field for the two situations shown in Fig. 10; all other cases can be treated by minor modifications of the following results.

For $0 \le H < H_m$ and *decreasing* field H we have to solve the equations

$$\frac{dB_m}{dr} = \frac{4\pi\mu_{cer}}{c} j_0 \left(1 - \frac{B_m}{B^*}\right), \quad r_m < r \le r_i ,$$

$$\frac{dB_i}{dr} = -\frac{4\pi\mu_{cer}}{c} j_0 \left(1 - \frac{B_i}{B^*}\right), \quad r_i < r \le R ,$$

together with the boundary conditions

$$B_m(R) = \mu_{cer} H_m ,$$

$$B_i(R) = \mu_{cer} H ,$$

$$B_m(r_m) = 0 ,$$

$$B_m(r_i) = B_i(r_i) .$$

The parameters r_m and r_i describe the penetration depth of the magnetic field and the position of current reversal, respectively (see Fig. 10). The solution of the differential equation is

$$B(r) = \begin{cases} B^*(1 - e^{\alpha(R-r)}) + \mu_{cer} H_m e^{\alpha(R-r)}, & r_m < r \le r_i , \\ B^*(1 - e^{-\alpha(R-r)}) + \mu_{cer} H e^{-\alpha(R-r)}, & r_i < r \le R , \end{cases}$$

with

$$R-r_m=\frac{1}{\alpha}\ln\frac{B^*}{B^*-\mu_{cer}H_m},$$

$$R-r_i=\frac{1}{2\alpha}\ln\frac{B^*-\mu_{cer}H}{B^*-\mu_{cer}H_m}.$$

For $-H_m<H<0$ and *decreasing* field H the differential equations to solve are

$$\frac{dB_m}{dr}=\frac{4\pi\mu_{cer}}{c}j_0\left[1-\frac{B_m}{B^*}\right],\quad r_m<r\le r_i,$$

$$\frac{dB_i}{dr}=-\frac{4\pi\mu_{cer}}{c}j_0\left[1-\frac{B_i}{B^*}\right],\quad r_i<r\le r_0,$$

$$\frac{dB_0}{dr}=-\frac{4\pi\mu_{cer}}{c}j_0\left[1+\frac{B_0}{B^*}\right],\quad r_0<r\le R,$$

and the boundary conditions read

$$B_m(R)=\mu_{cer}H_m,\ B_i(r_0)=0,\ B_0(R)=\mu_{cer}H,$$

$$B_m(r_m)=0,\ B_m(r_i)=B_i(r_i),\ B_0(r_0)=0.$$

In addition to the penetration depth r_m and the inversion radius r_i, a third radius r_0 describes the position of the maximal current density in the sample (see Fig. 10). The solution for the magnetic induction is

$$B(r)=\begin{cases}B^*(1-e^{\alpha(R-r)})+\mu_{cer}H_m e^{\alpha(R-r)}, & r_m<r\le r_i,\\ B^*(1-e^{-\alpha(r_0-r)}), & r_i<r\le r_0,\\ B^*(e^{\alpha(R-r)}-1)+\mu_{cer}He^{\alpha(R-r)}, & r_0<r\le R\end{cases}$$

with

$$R-r_m=\frac{1}{\alpha}\ln\frac{B^*}{B^*-\mu_{cer}H_m},$$

$$R-r_i=\frac{1}{2\alpha}\ln\left[\frac{B^*}{B^*-\mu_{cer}H_m}\frac{B^*}{B^*+\mu_{cer}H}\right],$$

$$R-r_0=\frac{1}{\alpha}\ln\frac{B^*}{B^*+\mu_{cer}H}.$$

The magnetization $4\pi M$ is obtained by averaging the field $B(r)$ over the sample volume, Eq. (9). The result is for $0\le J<H_m$:

$$\langle B\rangle=B^*\left[1-\frac{r_m^2}{R^2}\right]+\frac{2}{(\alpha R)^2}(B^*-\mu_{cer}H_m)[(1+\alpha r_i)e^{\alpha(R-r_i)}-(1+\alpha r_m)e^{\alpha(R-r_m)}]$$

$$+\frac{2}{(\alpha R)^2}(B^*-\mu_{cer}H)[(1-\alpha R)-(1-\alpha r_i)e^{-\alpha(R-r_i)}],$$

for $-H_m<H<0$:

$$\langle B\rangle=B^*\left[\frac{2r_0^2}{R^2}-\frac{r_m^2}{R^2}-1\right]+\frac{2}{(\alpha R)^2}(B^*-\mu_{cer}H_m)[(1+\alpha r_i)e^{\alpha(R-r_i)}-(1+\alpha r_m)e^{\alpha(R-r_m)}]$$

$$-\frac{2}{(\alpha R)^2}(B^*+\mu_{cer}H)[(1+\alpha R)-(1+\alpha r_0)e^{\alpha(R-r_0)}]+\frac{2}{(\alpha R)^2}B^*[(1-\alpha r_0)-(1-\alpha r_i)e^{-\alpha(r_0-r_i)}].$$

We make two final remarks: (i) As the field penetrates further into the sample, r_m (and thus also r_i and r_0) becomes 0. The penetration depth $R-r_m$ is, therefore, always meant to read

$$R-r_m=\min\left[R,\frac{1}{\alpha}\ln\frac{B^*}{B^*-\mu_{cer}H_m}\right]$$

and similar expressions apply to $R-r_i$ and $R-r_0$. With this proviso the obtained formulas apply to all field strengths $H_m<B^*/\mu_{cer}$. Increasing the maximal field beyond B^*/μ_{cer} the sample behaves again reversible and is diamagnetic, $4\pi M=-(1-\mu_{cer})H$. As H drops back below B^*/μ_{cer} the above results can be applied with $H_m=B^*/\mu_{cer}$. (ii) When the magnetic field H is *increased* from a value $-H_m$, $H_m>0$, all the above formulae apply with B^* and H_m substituted by $-B^*$ and $-H_m$, respectively.

[1]A. Raboutou, J. Rosenblatt, and P. Peyral, Phys. Rev. Lett. **45**, 1035 (1980).

[2]A. Raboutou, P. Peyral, J. Rosenblatt, C. Lebeau, O. Peña, A. Perrin, C. Perrin, and M. Sergent, Europhys. Lett. **4**, 1321 (1987).

[3]C. Ebner and D. Stroud, Phys. Rev. B **31**, 165 (1985).

[4]John R. Clem, B. Bumble, S. I. Raider, W. J. Gallagher, and Y. C. Shih, Phys. Rev. B **35**, 6637 (1987).

[5]C. J. Lobb, D. W. Abraham, and M. Tinkham, Phys. Rev. B **27**, 150 (1983).

[6]B. D. Josephson, in *Superconductivity, Vol. 1,* edited by R. D. Parks (Marcel Dekker, New York, 1969), p. 423; J. E. Mercereau, *ibid*, p. 393.

[7]C. P. Bean, Phys. Rev. Lett. **8**, 250 (1962); Rev. Mod. Phys. **36**, 31 (1964).

[8]M. N. Wilson, *Superconducting Magnets,* edited by R. G.

Scurlock (Clarendon, Oxford, 1983).
[9]H. Kumakura, M. Uehara, and K. Togano, Appl. Phys. Lett. **51**, 1557 (1987).
[10]K. Funaki, M. Iwakuma, Y. Sudo, B. Ni, T. Kisu, T. Matsushita, M. Takeo, and K. Yamafuji, Jpn. J. Appl. Phys. **26**, L1445 (1987).
[11]H. Küpfer, I. Apfelstedt, W. Schauer, R. Flückiger, R. Meier-Hirmer, and H. Wühl, Z. Phys. B **69**, 159 (1987).
[12]J. W. Ekin, T. M. Larson, N. F. Bergren, A. J. Nelson, A. B. Swartzlander, L. L. Kazmerski, A. J. Panson, and B. A. Blankenship, Appl. Phys. Lett. **52**, 1819 (1988).
[13]I. Sugimoto, Y. Tajima, and M. Hikita, Jpn. J. Appl. Phys. **27**, L864 (1988).
[14]Y. Tzeng, A. Holt, and R. Ely, Appl. Phys. Lett. **52**, 155 (1988).
[15]J. Rosenblatt, P. Peyral, and A. Raboutou, in *Inhomogeneous Superconductors 1979,* AIP Conf. Proc. No. 58, edited by D. U. Gubser, T. L. Francavilla, S. A. Wolf, and J. R. Leibowitz (American Institute of Physics, New York, 1980), p. 33 and p. 272.
[16]J. W. Ekin, A. I. Braginski, A. J. Panson, M. A. Janocko, D. W. Capone II, N. J. Zaluzec, B. Flandermeyer, O. F. de Lima, M. Hong, J. Kwo, and S. H. Liou, J. Appl. Phys. **62**, 4821 (1987).
[17]The local current density j_c is expected to depend on the local magnetic induction B which we want to distinguish from the applied magnetic field denoted by H.
[18]A. Umezawa, G. W. Crabtree, J. Z. Liu, T. J. Moran, S. K. Malik, L. H. Nunez, W. L. Kwok, and C. H. Sowers, Phys. Rev. B **38**, 2843 (1988).
[19]A. L. Fetter and P. C. Hohnenberg, in *Superconductivity, Vol. 2,* edited by R. D. Parks (Marcel Dekker, New York, 1969), p. 817.
[20]D. Saint-James, G. Sarma, and E. J. Thomas, in *Type II Superconductivity, Vol. 13,* edited by D. ter Haar (Pergamon, Oxford, 1969), p. 134.
[21]S. A. Solin, N. Garcia, S. Vieira, and M. Hortal, Phys. Rev. Lett. **60**, 744 (1988).
[22]M. Abramowitz and I. A. Stegun, *Handbook of Mathematical Functions* (Dover, New York, 1965).
[23]J. R. Cooper, C. T. Chu, L. W. Zhou, B. Dunn, and G. Grüner, Phys. Rev. B **37**, 638 (1988).
[24]Here we describe the transition from the uncoupled superconducting state to the coupled coherent state. The reference state is, therefore, the uncoupled superconducting state which has a magnetic energy $B^2/8\pi\mu_{cer}$. This is the reason why the permeability μ_{cer} of the ceramic enters the expression.
[25]T. K. Worthington, W. J. Gallagher, and T. R. Dinger, Phys. Rev. Lett. **59**, 1160 (1987).
[26]M. Gurvitch and A. T. Fiory, Phys. Rev. Lett. **59**, 1337 (1987).
[27]P. W. Anderson, Phys. Rev. Lett. **9**, 309 (1962).
[28]Y. B. Kim, C. F. Hempstead, and A. R. Strnad, Phys. Rev. Lett. **9**, 306 (1962).
[29]R. L. Peterson and J. W. Ekin, Phys. Rev. B **37**, 9848 (1988).
[30]J. F. Kwak, E. L. Venturini, P. J. Nigrey, and D. S. Ginley, Phys. Rev. B **37**, 9749 (1988).
[31]A. R. Strnad, C. F. Hempstead, and Y. B. Kim, Phys. Rev. Lett. **13**, 794 (1964).